IOP Publishing Nanotechnology
Nanotechnology 30 (2019) 324005 (5pp) https://doi.org/10.1088/1361-6528/aaf9ce

Composition modulation by twinning in InAsSb nanowires

M Schnedler[1], T Xu[2,3], V Portz[1], J-P Nys[2], S R Plissard[2,4], M Berthe[2], H Eisele[5], R E Dunin-Borkowski[1], P Ebert[1] and B Grandidier[2]

[1] Peter Grünberg Institut, Forschungszentrum Jülich GmbH, D-52425 Jülich, Germany
[2] Université de Lille, CNRS, Centrale Lille, ISEN, Université de Valenciennes, UMR 8520 - IEMN, F-59000 Lille, France
[3] Key Laboratory of Advanced Display and System Application, Shanghai University, 149 Yanchang Road, Shanghai 200072, People's Republic of China
[4] Laboratoire d'Analyse et d'Architecture des Systèmes (LAAS), CNRS, Université de Toulouse, 7 Avenue du Colonel Roche, F-31400 Toulouse, France
[5] Institut für Festkörperphysik, Technische Universität Berlin, Hardenbergstr. 36, D-10623 Berlin, Germany

E-mail: bruno.grandidier@isen.iemn.univ-lille1.fr

Received 24 October 2018, revised 10 December 2018
Accepted for publication 19 December 2018
Published 21 May 2019

Abstract

We observe a composition modulated axial heterostructure in zincblende (ZB) $InAs_{0.90}Sb_{0.10}$ nanowires initiated by pseudo-periodic twin boundaries using scanning tunneling microscopy. The twin boundaries exhibit four planes with reduced Sb concentration due to a lower Sb incorporation during lateral overgrowth of a 4H wurtzite as compared to a ZB stacking sequence. We anticipate that this leads to compositional band offsets in addition to known structural band offsets present between 4H and ZB polytypes, changing the band alignment from type II to type I.

Keywords: semiconductor nanowires, composition modulation, twin boundaries, scanning tunneling microscopy, ternary III–V compounds

(Some figures may appear in colour only in the online journal)

1. Introduction

Ternary III–V compound semiconductor nanowires (NWs) are promising building blocks for nanoscale electronic and photonic devices. Due to their one-dimensional morphology, NWs can be grown with almost any alloy composition without detrimental lattice mismatch effects, in sharp contrast to thin film growth. This offers an ultimate engineering of material properties such as band gaps or band alignments [1, 2].

The growth of NWs is mostly based on vapor–liquid–solid process [3], where a catalyst droplet governs the structure and morphology of the NW [4]. Ideally the axial layer by layer growth takes place at the catalyst-NW interface with constant diameter. However, for zincblende (ZB) structure NWs oscillations of the shape and size of the catalyst-NW interface as well as the contact angle between the $\{\overline{1}11\}$ growth surface and the surface of the seed droplet lead frequently to the formation of pseudo-periodic twin boundaries, equivalent to insertions of wurtzite (WZ) structure bilayers [5, 6]. These planar defects can influence carrier transport, band structure, photonic properties, and/or polarization [7, 8]. For example direct band gaps can be created by pseudo-periodic twin boundaries in indirect band gap material NWs [9].

Furthermore the crystal structure of NWs can be controlled to a large degree by growth conditions and alloy composition [10–15], even though only one structure is stable in the bulk/thin films: III–V materials with large ionicity and atom size differences (i.e. nitrides [16], phosphides [17], and partially arsenides [18]) preferentially form WZ structure NWs, whereas materials with smaller differences form the ZB structure NWs (i.e. antimonides [19]). One example is the crystal structure of $InAs_{1-x}Sb_x$ NWs that changes from WZ to ZB at Sb concentrations of about 3% [19, 20]. Alloying with different group V atoms can hence change the preferred

 © 2019 IOP Publishing Ltd Printed in the UK

crystal structure and in return the crystal structure may influence the alloy composition. Therefore, the question arises how twin boundaries affect the local composition of ternary III–V NWs. This is particularly critical, since pseudo-periodic twin boundaries could lead to a periodic composition modulation of ternary III–V NWs, which affects the electronic properties much more directly than a possible local defect state associated with the twin boundary.

Here, we investigate the spatial fluctuations of the alloy composition in pseudoperiodically twinned $InAs_{0.90}Sb_{0.10}$ NWs by scanning tunneling microscopy (STM). We identify the spontaneous formation of a composition modulated In(As, Sb) axial heterostructure governed by twinning of $InAs_{0.90}Sb_{0.10}$ NWs. The driving mechanism is the reduced Sb incorporation rate in WZ-type layers present at the twin boundary during lateral overgrowth. We anticipate that this offers new degrees of freedom to create novel periodic compositional heterostuctures, with tailored band offsets and novel electronic properties.

2. Experiment

For our investigations we used ZB $InAs_{0.90}Sb_{0.10}$ NW segments grown on top of WZ InAs NWs in $[\bar{1}\,\bar{1}\,\bar{1}]$ direction by Au droplet assisted gas source molecular beam epitaxy at a temperature of 410 °C. Detailed information about the growth parameters and Sb composition analysis can be found in [19, 21]. To prevent oxidation during the transfer through air from the growth chamber to the STM-UHV system, the NWs were capped after growth by a protective layer of arsenic. This arsenic cap was thermally desorbed at 350 °C in the STM-UHV system. Capping and decapping do neither change the Sb concentration and distribution profile nor influence the morphology of the NWs [19, 22]. After decapping, the clean NWs were cleaved-off and transferred to a clean Si(111) 7 × 7 surface for STM investigation.

3. Results

3.1. Atomic structure of twin boundaries

A schematic drawing of the investigated NWs is presented in figure 1(a). The bottom WZ InAs segment, shown in blue, consists initially of six equivalent non-polar $\{10\bar{1}0\}$ sidewall facets, changing into $\{11\bar{2}0\}$ facets with progressing growth. The top ZB segment, shown in red, also exhibits a six-fold symmetry with six non-polar {110} sidewalls. Additionally, a sawtooth faceting at the edges of two adjacent {110} sidewall facets is observed. This sawtooth faceting is connected to pseudo-periodic twin boundaries [19]. In the following, these twin boundaries are analyzed by STM.

Figure 1(b) shows an atomically resolved constant-current STM image of a ZB $InAs_{0.90}Sb_{0.10}$ NW sidewall facet, measured at 77 K and a sample voltage of −2 V. At these measurement conditions, the contrast in the STM image is given by the filled dangling bond states above the surface

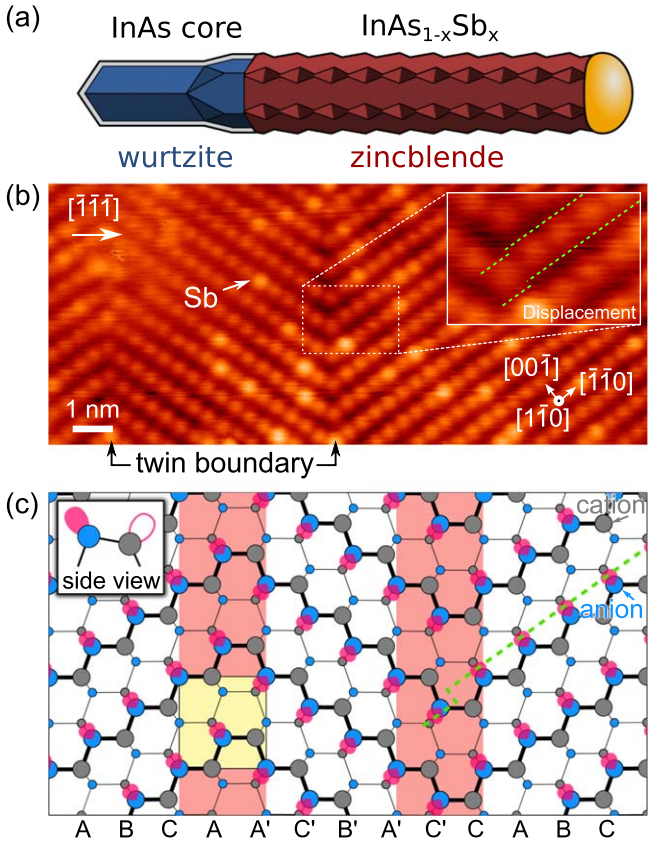

Figure 1. (a) Schematic of the zincblende $InAs_{1-x}Sb_x$ nanowire (red), grown on top of wurtzite InAs nanowire (blue) in $[\bar{1}\bar{1}\bar{1}]$ direction. During the growth of the top part, a lateral overgrowth of the InAs bottom part can be observed. (b) Atomically resolved constant-current STM image of two twin boundaries at the $InAs_{0.90}Sb_{0.10}$ NW sidewall measured at 77 K (−2 V sample voltage and 700 pA tunnel current). The image shows the filled dangling bond states above the surface anions. The bright atomically localized contrast features arise from Sb atoms incorporated on anion sites. Inset: magnification of one of the twin boundaries. One chain of dangling bonds in $[\bar{1}10]$ direction is marked by green dashed lines. If one traces this chain back to the twin boundary, the dangling bond imaged directly at the boundary exhibits a slight downward displacement. The displacement implies a directional change of the dangling bond at the twin boundary. (c) Ball-model of the ZB atomic lattice of the {110} NW sidewall facet including two twin boundaries (red shaded areas). In (As) atoms of the first and second atomic layer are represented by filled gray (blue) circles. The dangling bonds of the As atoms in the first atomic layer are shown as red ellipsoids. For the formation of a twin boundary, the insertion of a single WZ layer is necessary. The *a*-plane unit cell of the WZ layer is shown by the yellow shaded rectangle. Inset: side view along [110] direction, showing the orientation of both, filled (red filled ellipse) and empty (empty ellipse) dangling bonds at the anions and cations, respectively.

anions [23]. Hence, only every second atom [i.e. all anions] of the characteristic anion–cation zigzag chains in ⟨110⟩ direction are imaged (see blue atoms in figure 1(c)). The NW sidewall area depicted in figure 1(b) exhibits three domains separated by two twin boundaries. The twin boundaries are stacking faults in the ABC stacking sequence of the ZB atomic lattice along the $[\bar{1}\bar{1}\bar{1}]$ direction. A corresponding schematic ball-model illustrating this domain and twin boundary structure is illustrated in figure 1(c). Large filled

gray and blue circles represent first layer cations (In) and anions (As, Sb), respectively, while small circles refer to second layer atoms. The twin boundaries are highlighted by the red shaded areas and exhibit ABC-AA′-C′B′A′ and C′B′A′-C′C-ABC stacking sequences, respectively. The insertion of an additional stacking layer leads to a rotation of the atomic lattice by 180° along the $[\bar{1}\bar{1}\bar{1}]$ direction.

At this stage we concentrate on the first layer atoms. Above every first layer anion and cation a filled and empty dangling bond surface state is present, respectively (see side view in the inset of figure 1(c)) [24]. Since the STM image shows the filled density of states, we only indicated the filled dangling bonds at the anions as red ellipses. These filled dangling bonds are inclined towards the ⟨001⟩ direction [25]. At the twin boundary, the orientation of the filled dangling bonds is rotated, leading to a small perpendicular displacement (see green dashed line highlighting the alignment of the red ellipses in figure 1(c)). This displacement is characteristic of twin stacking sequences [26, 27] and can be observed in the magnified STM image shown as inset of figure 1(b): when tracing the atomic chains from the right side towards the twin boundary, a slight downward displacement of the lowermost dangling bond directly at the twin boundary can be observed, as highlighted by the green dashed lines, in perfect agreement with the ball-model. The above mentioned AB[C-A-A′]C′B′ and C′B′[A′-C′-C]AB stacking sequences at the twin boundaries correspond to the local insertion of two WZ structure planes. This is indicated by the WZ *a*-plane unit cell highlighted by a yellow rectangle in figure 1(c).

3.2. Sb composition modulation

After characterizing the atomic structure of the NW, we turn to the chemical analysis. For this, we make use of the fact that Sb atoms incorporated substitutionally on anion surface sites appear as bright, atomically-sized protrusions in the STM images [21, 28]. On this basis, we identify the atomic lattice position of every Sb atom in STM images and determine the local Sb concentration. A map of the local Sb concentration of the {110} ZB structure NW sidewall facet, together with the corresponding STM image, is shown in figures 2(a) and (b), respectively. The positions of the twin boundaries are indicated by white dashed lines. At first glance, the surface Sb concentration in figure 2(a) seems to fluctuate between 0.3 and 1.8 nm^{-2}, forming clusters with higher Sb concentrations around 25%. However, along the twin boundaries, rather low Sb concentrations are observed.

This first indication of a correlation between the Sb concentration and the twin boundary positions is further corroborated by evaluating the Sb concentration $c(x) = \frac{n_{Sb}(x)}{n_{Sb}(x)+n_{As}(x)}$ in every atomic row parallel to the twin boundary [equivalent to every $(\bar{1}\bar{1}\bar{1})$ layer] as a function of the distance x to the twin boundary. $n_{Sb}(x)$ and $n_{As}(x)$ denote the number of Sb and As atoms, respectively. In addition, we normalized the layer resolved Sb concentration by the overall average Sb concentration $c_0 = \frac{N_{Sb}}{N_{Sb}+N_{As}}$, where N_{Sb} as well as N_{As} are the total numbers of Sb and As atoms of the investigated domain,

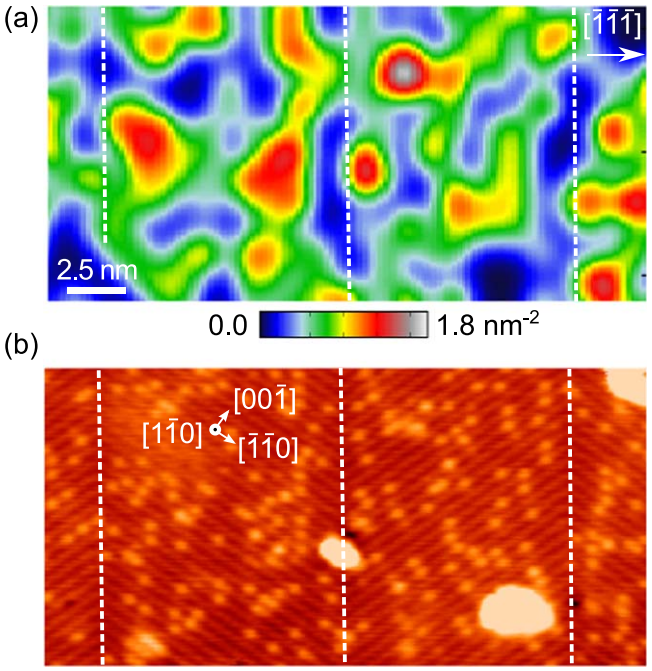

Figure 2. (a) Local Sb surface concentration map derived from the STM image shown in (b). (b) Atomically resolved constant-current STM image of the sidewall surface measured at 77 K (−3 V sample voltage and 10 pA tunnel current). The image shows the filled dangling bond states above the surface anions. The atomically-sized protrusions arise from Sb atoms incorporated on anion sites. Twin boundaries are marked by dashed vertical lines.

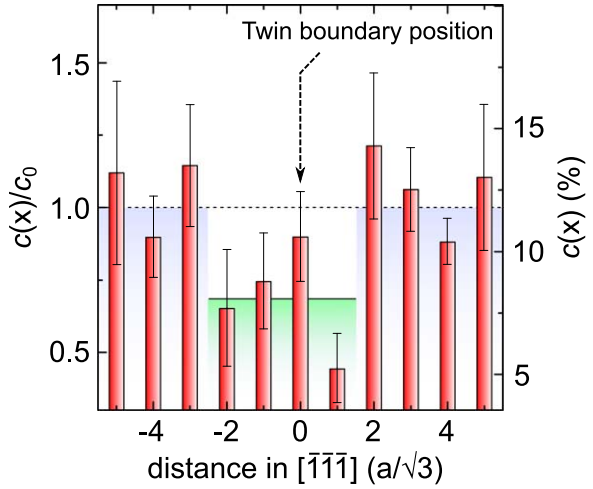

Figure 3. Normalized, plane-resolved concentration $c(x)$ of Sb atoms in $InAs_{0.90}Sb_{0.10}$ NWs as a function of the distance x to a twin boundary. The concentrations were measured in STM images of the {110} sidewall facet. Values above (below) 1 indicate a higher (lower) than statistically expected occurrence of Sb. Four atomic planes round the twin boundary exhibit a significantly smaller Sb concentration than statistically expected (see green shaded area) The average normalized Sb concentration near the twin boundary is 0.68 ± 0.1, corresponding to $InAs_{0.92}Sb_{0.08}$.

respectively. We derived the Sb concentration $c(x)$ from STM images of the sidewall facet for seven different domains, corresponding to ∼5000 atoms in total. The bar chart in figure 3 illustrates the spatial distribution of the Sb

concentration averaged over the seven domains. The twin boundary position is at $x = 0$. Close to the twin boundary four atomic planes exhibit a Sb concentration significantly lower than the overall average $c_0 = 11.8\%$. The normalized Sb concentration of these four atomic planes near the twin boundaries is on average 0.68 ± 0.1 (i.e. $InAs_{0.92}Sb_{0.08}$), as indicated by the green shaded bar in the background of figure 3.

4. Discussion

4.1. Sb incorporation

The experimental Sb concentration measurement in figure 3 demonstrates that the incorporation of Sb is less favorable near the twin boundary as compared to the center of the individual ZB domains. This effect can be correlated with the presence of a WZ-type stacking at the twin boundary.

For demonstrating this we recall that during growth of the nominal $InAs_{0.90}Sb_{0.10}$ segment, the bottom WZ structure InAs segment is laterally overgrown by In(As, Sb), which inherits the WZ structure of the InAs core [19]. STM images of this WZ structure In(As, Sb) shell show that the Sb concentration is only (8.2 ± 1) % on the WZ structure *m*-plane sidewall facet, i.e. much lower than on the ZB (110) facet, grown simultaneously under identical conditions. Note, the sidewalls of both segments represent surfaces formed by lateral overgrowth [21]. Furthermore, imaging of *m* and *a*-plane facets of other In(As, Sb) NWs with slightly higher Sb concentration (not shown here) demonstrate that the Sb incorporation is almost identical on WZ structure *m* and *a*-plane facets. Hence, the lower Sb incorporation is not a surface orientation effect during lateral overgrowth, but is related to the incorporation of Sb in the WZ structure itself [29]. Indeed, alloying InAs NWs with Sb induces, at very low Sb concentrations, a switch from WZ to ZB structure in axial growth [11, 19, 30]. This axial switch can also be interpreted as lower solubility of Sb in WZ structure InAs than in ZB structure InAs. Hence, the Sb incorporation is lower on WZ structure than on ZB structure shells and similar effects can be expected in the core of the NW. This explains the observation of a reduced Sb concentration near twin boundaries.

4.2. Implication on band offsets

At this stage we address the electronic effects of the composition changes near twin boundaries. Changing the Sb composition is inevitably connected to changes of the band gap and insertions of band offsets. To illustrate this we derived the layer by layer resolved band edge positions using our measured Sb compositions $c(x)$ and the $InAs_{1-x}Sb_x$ bowing parameters determined in [31]. Figure 4 shows the such obtained conduction and valence band edge positions determined for the layer resolved Sb compositions shown in figure 3 as white symbols. Considering only the compositional effects, no band offset is present for the conduction band, since the bowing of the conduction band edge is flat for the here present composition range. In contrast, the bowing of the valence band edge is steep with composition and hence the valence band edge is found to be lower for four layers near the twin boundary.

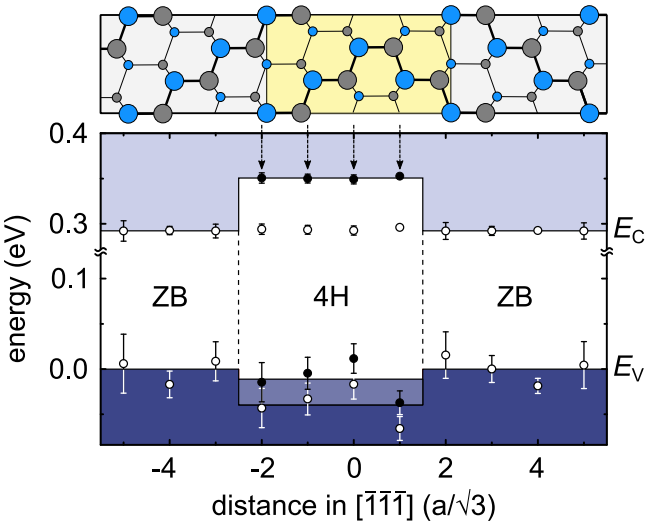

Figure 4. Conduction and valence band edge positions determined for the measured Sb compositions shown in figure 3 using the Sb composition bowing parameters of $InAs_{1-x}Sb_x$ given in [31] (white symbols). In addition, near the twin boundary, the stacking corresponds to a 4H wurtzite structure insertion, which additionally has band offsets with the surrounding zincblende structure [34]. This shifts the band edge positions upward, changing the almost flat band condition from the conduction to the valence band (see filled symbols). The averaged band alignment is indicated by the background shading.

This raises the question how to relate these four layers to the stacking sequence, as only two WZ-type layers are inserted at a twin boundary (see figure 1(c)). At closer look, the stacking sequence near the twin boundary can also be considered as a 4H type wurtzite structure insertion (see figure 1(c)). The corresponding surface unit cell is highlighted as yellow shaded area in the schematic model in figure 4. This view is supported by the fact that an inserted 4H unit cell naturally affects four layers and 4H segments were also previously found in III–V NWs [32, 33]. Hence, the experimental data suggest that a ZB twin boundary behaves electrically like a 4H insertion.

Besides the thus far discussed compositional band offsets, a 4H wurtzite structure insertion has also structurally induced band offsets. These band offsets with respect to the surrounding ZB structure were calculated to be 29 and 58 meV for the valence and conduction band, respectively [34], shifting the band edge positions in the 4H segment upward. Therefore, as first approximation of the total compositionally and structurally induced band structure at the twin boundary, we added the structural 4H-ZB band offsets to the compositional band edge positions values in figure 4 for the four layers at the twin boundary (filled black circles).

Furthermore, the background shading in figure 4 indicates the average band edge energies for the 4H insertion and the surrounding zincblende structure. Note, the subatomic potential shape of the band offset at the interface cannot be

deduced here, since the band edge energies are only (111) bilayer resolved. However, the averaged band alignment reveals a type I band alignment (with large positive conduction band and small negative valence band offset) in contrast to the type II band alignment expected for pure InAs 4H-ZB (or WZ-ZB) polytype interfaces without additional composition modulation. Hence, the transition from type II to type I band alignment results from the Sb composition modulation at the twin boundaries.

5. Conclusions

In conclusion, twin boundaries in ZB $InAs_{0.90}Sb_{0.10}$ NWs exhibit four planes with reduced Sb concentration due to a lower Sb incorporation during lateral overgrowth of a 4H stacking sequence as compared to a ZB one. This reduced incorporation is also found for lateral overgrowth of 2H wurtzite stacking sequences. The twin boundary-induced compositional modulation introduces compositional band offsets in addition to structural ones between 4H and ZB polytypes. Thereby the type II band alignment between 4H-ZB transforms into a type I band alignment. Hence, the insertion of twin boundaries has a much deeper impact on the electronic properties of NWs than just localized defect states and offers the possibility to create composition modulated heterostructures.

Acknowledgments

The authors thank P Caroff for the growth of the nanowires. This study was financially supported by the European Community's Horizon H2020 Program (Grant No. PITN-GA-2016-722176, 'Indeed' Project), the EQUIPEX program Excelsior (Grant No. ANR-11-EQPX-0015), the RENATECH network, and the Deutsche Forschungsgemeinschaft (DFG, German Research Foundation) (Grant No. 390247238).

ORCID iDs

S R Plissard https://orcid.org/0000-0002-0769-5429
B Grandidier https://orcid.org/0000-0001-6131-7309

References

[1] Xiang H J, Wei S H, Da Silva J L F and Li J 2008 *Phys. Rev.* B **78** 193301
[2] Dick K A 2008 *Prog. Cryst. Growth Charact. Mater.* **54** 138–73
[3] Wagner R S and Ellis W C 1964 *Appl. Phys. Lett.* **4** 89–90
[4] Jia S, Hu S, Zheng H, Wei Y, Meng S, Sheng H, Liu H, Zhou S, Zhao D and Wang J 2018 *Nano Lett.* **18** 4095–9
[5] Davidson F M, Lee D C, Fanfair D D and Korgel B A 2007 *J. Phys. Chem.* C **111** 2929–35
[6] Wang F, Wang C, Wang Y, Zhang M, Han Z, Yip S, Shen L, Han N, Pun E Y B and Ho J C 2016 *Sci. Rep.* **6** 32910
[7] Capiod P *et al* 2013 *Appl. Phys. Lett.* **103** 122104
[8] Li L, Gan Z, McCartney M R, Liang H, Yu H B, Yin W J, Yan Y, Gao Y, Wang J and Smith D J 2014 *Adv. Mater.* **26** 1052–7
[9] Yeh C Y, Wei S H and Zunger A 1994 *Phys. Rev.* B **50** 2715–8
[10] Caroff P, Dick K A, Johansson J, Messing M E, Deppert K and Samuelson L 2009 *Nat. Nanotechnol.* **4** 50–5
[11] Gorji Ghalamestani S, Lehmann S and Dick K A 2016 *Nanoscale* **8** 2778–86
[12] Lehmann S, Wallentin J, Jacobsson D, Deppert K and Dick K A 2013 *Nano Lett.* **13** 4099–105
[13] Bolinsson J, Caroff P, Mandl B and Dick K A 2011 *Nanotechnology* **22** 265606
[14] Dick K A, Caroff P, Bolinsson J, Messing M E, Johansson J, Deppert K, Wallenberg L R and Samuelson L 2010 *Semicond. Sci. Technol.* **25** 024009
[15] Wood E L and Sansoz F 2012 *Nanoscale* **4** 5268–76
[16] Avit G, Lekhal K, André Y, Bougerol C, Réveret F, Leymarie J, Gil E, Monier G, Castelluci D and Trassoudaine A 2014 *Nano Lett.* **14** 559–62
[17] Mohammad R and Katırcıoğlu Ş 2015 *Physica* E **73** 213–9
[18] Spirkoska D *et al* 2009 *Phys. Rev.* B **80** 245325
[19] Xu T, Dick K A, Plissard S, Nguyen T H, Makoudi Y, Berthe M, Nys J P, Wallart X, Grandidier B and Caroff P 2012 *Nanotechnology* **23** 095702
[20] Ercolani D, Gemmi M, Nasi L, Rossi F, Pea M, Li A, Salviati G, Beltram F and Sorba L 2012 *Nanotechnology* **23** 115606
[21] Schnedler M *et al* 2016 *Phys. Rev.* B **94** 195306
[22] Xu T and Grandidier B 2015 Electrical characterization of semiconductor nanowires by scanning probe microscopies *Semiconductor Nanowires: Materials, Synthesis, Characterization and Applications* ed J Arbiol and Q Xiong vol 77 (Amsterdam: Elsevier) pp 277–304
[23] Feenstra R M and Stroscio J A 1987 *J. Vac Sci. Technol.* B **5** 923–9
[24] Chelikowsky J and Cohen M 1979 *Solid State Commun.* **29** 267–71
[25] Engels B, Richard P, Schroeder K, Blügel S, Ebert P and Urban K 1998 *Phys. Rev.* B **58** 7799–815
[26] Cox G, Szynka D, Poppe U, Graf K H, Urban K, Kisielowski-Kemmerich C, Krüger J and Alexander H 1990 *Phys. Rev. Lett.* **64** 2402–5
[27] Bolinsson J, Ouattara L, Hofer W A, Sköld N, Lundgren E, Gustafsson A and Mikkelsen A 2009 *J. Phys.: Condens. Matter* **21** 055404
[28] Steinshnider J, Harper J, Weimer M, Lin C H, Pei S S and Chow D H 2000 *Phys. Rev. Lett.* **85** 4562–5
[29] Hjort M, Kratzer P, Lehmann S, Patel S J, Dick K A, Palmstrøm C J, Timm R and Mikkelsen A 2017 *Nano Lett.* **17** 3634–40
[30] Caroff P, Wagner J B, Dick K A, Nilsson H A, Jeppsson M, Deppert K, Samuelson L, Wallenberg L R and Wernersson L 2008 *Small* **4** 878–82
[31] Webster P T, Riordan N A, Liu S, Steenbergen E H, Synowicki R A, Zhang Y H and Johnson S R 2015 *J. Appl. Phys.* **118** 245706
[32] Dheeraj D L, Patriarche G, Zhou H, Hoang T B, Moses A F, Grønsberg S, van Helvoort A T J, Fimland B O and Weman H 2008 *Nano Lett.* **8** 4459–63
[33] Jacobsson D, Yang F, Hillerich K, Lenrick F, Lehmann S, Kriegner D, Stangl J, Wallenberg L R, Dick K A and Johansson J 2015 *Cryst. Growth Des.* **15** 4795–803
[34] Bechstedt F and Belabbes A 2013 *J. Phys.: Condens. Matter* **25** 273201